Hyperspectral Image Classification Using Fast and Adaptive Bidimensional Empirical Mode Decomposition With Minimum Noise Fraction

Ming-Der Yang, Kai-Shiang Huang, Yeh Fen Yang, Liang-You Lu, Zheng-Yi Feng, and Hui Ping Tsai

***Abstract*—The scattered pixel problem in hyperspectral images caused by atmospheric noises and incomplete classification can lead to unsatisfactory classification; this problem remains to be solved. This letter reports the application of minimum noise fractions (MNFs) combined with fast and adaptive bidimensional empirical mode decomposition (FABEMD) as a two-step process to improve the classification accuracy of airborne visible–infrared imaging spectrometer hyperspectral image of the Indian Pine data set. With dimensional reduction by using MNF, FABEMD, considered as a low-pass filter, decomposes a hyperspectral image into several bidimensional intrinsic mode functions (BIMFs) and a residue image. The first four BIMFs are removed and the remainder BIMFs are integrated to reconstruct informative images that are subsequently classified through a support vector machine classifier (SVM). The classification results show that the proposed approach can effectively eliminate noise effects and can obtain higher accuracy than does traditional MNF SVM.**

***Index Terms*—Empirical mode decomposition (EMD), fast and adaptive bidimensional EMD (FABEMD), hyperspectral image classification, minimum noise fraction (MNF), support vector machine (SVM).**

I. Introduction

Hyperspectral image technology for land-cover classification has improved tremendously [1]. Image classification techniques are broadly used on remote sensing images, and the classification value depends on their accuracy [2]–[5]. Environmental noise and classifier effects within hyperspectral images degrade classification accuracy that remains to be solved [6]. Noise detection and deletion trades off detail preservation against noise reduction within an image to reduce noise contained in an image [7]. Several methods, such as statistical filters [8], discrete Fourier transforms and wavelet estimation [9], [10], rotation forests [11], morphological segmentation [12], [13], and minimum noise fractions (MNFs) [14], were proposed to solve noise problems.

Manuscript received May 19, 2016; revised August 16, 2016; accepted September 30, 2016. Date of publication November 8, 2016; date of current version December 7, 2016. This work was supported by the Ministry of Science and Technology of Taiwan under Project MOST103-2625-M-005-008-MY2. *(Corresponding author: Hui Ping Tsai.)*

M.-D. Yang, K.-S. Huang, Y. F. Yang, L.-Y. Lu, and H. P. Tsai are with the Department of Civil Engineering, National Chung Hsing University, Taichung 402, Taiwan (e-mail: mdyang@nchu.edu.tw; d9762402@mail.nchu.edu.tw; yf.yang@yahoo.com.tw; a95207430@gmail.com; huiping.tsai@gmail.com).

Z.-Y. Feng is with the Department of Soil and Water Conservation, National Chung Hsing University, Taichung 402, Taiwan (e-mail: tonyfeng@nchu.edu.tw).

Color versions of one or more of the figures in this paper are available online at http://ieeexplore.ieee.org.

Digital Object Identifier 10.1109/LGRS.2016.2618930

Recently, empirical mode decomposition (EMD) was proposed as a 1-D signal decomposition method [15] and has been applied in many applications [16]–[18]. EMD decomposes an input signal into several hierarchical components known as intrinsic mode functions (IMFs) and a residue signal. As extensions of this concept, bidimensional EMD (BEMD) was introduced to process 2-D images [19], and fast and adaptive BEMD (FABEMD) was developed to improve the computational complexity of BEMD [20]. Support vector machine (SVM) classification is a well-known supervised learning classifier that has been applied on many research fields [21]–[26]. In a recent study, SVM hyperspectral image classification on the Indian Pine image using spectral and spatial information reached overall accuracy up to 97.24% [27].

This letter proposes a two-step (MNF and FABEMD) process involving spectral information for classifying hyperspectral images. The Airborne Visible–Infrared Imaging Spectrometer (AVIRIS) Indian Pine data set was used. MNF, and MNF-FABEMD images were fused into three image composites for comparison purpose in SVM classification.

II. Proposed Methodology

The flowchart of the proposed process is shown in Fig. 1. The goal is to extract sufficient information to enhance the hyperspectral classification accuracy. An MNF transform is executed as the first-step process, dimensional reduction. Sequentially, the 1st to the 14th MNFs are selected to compose three experimental image sets, namely, MNF1–5, MNF1–10, and MNF1–14. In the second-step process, image decomposition, the 14 selected MNF transformed images are subjected to FABEMD. Two to seven low-order bidimensional IMFs (BIMFs) are removed to minimize the influence of redundant classification information. Three experimental image sets—MNF-FABEMD 1–5, MNF-FABEMD 1–10, and MNF-FABEMD 1–14—are fused for SVM classification, and the classification results of MNF and MNF-FABEMD images are compared.

A. Minimum Noise Fraction

For dimensionality reduction, MNF segregates noise from informative data through modified principle component analysis by ranking images on the basis of SNR [28]. The MNF process defines a noise fraction of a band as follows:

$$\mathrm{Var}\{N_i(x)\}/\mathrm{Var}\{Z_i(x)\} \tag{1}$$

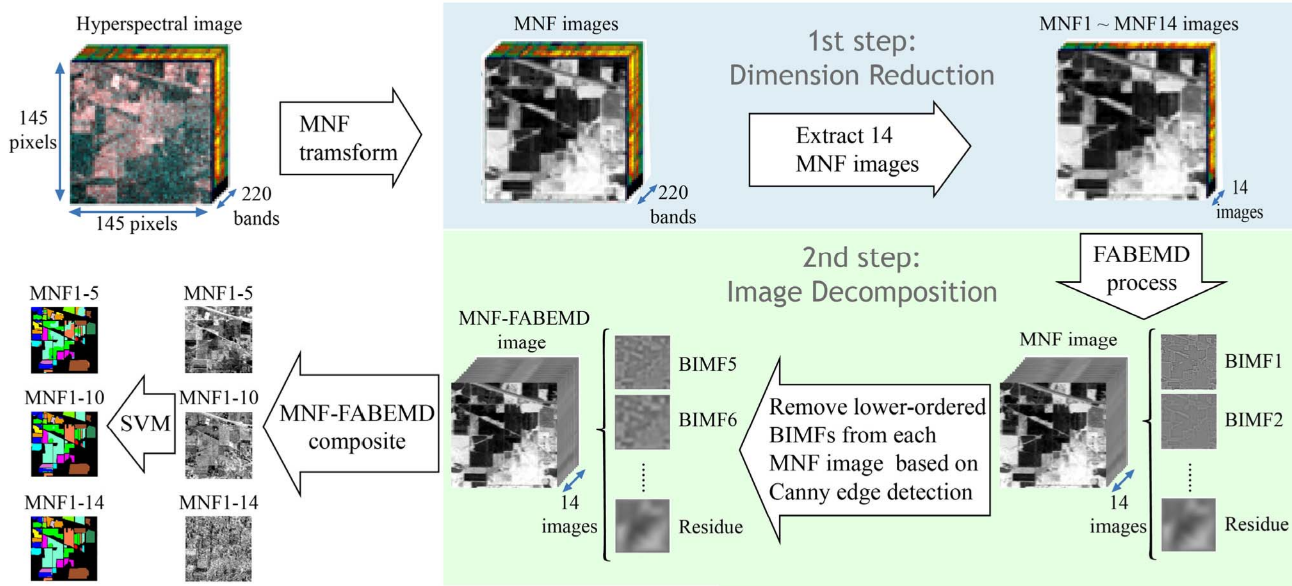

Fig. 1. Flowchart of the proposed two-step process.

where $N_i(x)$ is the noise content of the xth pixel in the ith band, and $Z_i(x)$ is the value of the corresponding pixel [9]. An image has p bands with gray levels, $Z_i(x)$, $i = 1, 2 \cdots, p$, where x is given as the image coordinate. A linear MNF transform is as follows:

$$Y_i(x) = a_i^T Z(x), \quad i = 1, \ldots, p \tag{2}$$

where a_i are the left-hand eigenfactors of $\Sigma_{N_i} \Sigma^{-1}$ and u_i are the corresponding eigenvalues of a_i equal to noise fraction in $Y_i(x)$. $u_1 \leq u_2 \leq \cdots \leq u$ explains the ranking of MNFs by image quality.

B. Support Vector Machine

An SVM classifier searches the largest distance between the classified data to the nearest training data points of any class and partitions the data set into two classes by using a hyperplane. The larger the distance, the lower the classification error [29]. The Gaussian radial basis function, a nonlinear model, is employed as

$$k(x_i, x_j) = \exp(-\gamma \|x_i - x_j\|^2), \quad \text{for } \gamma > 0 \tag{3}$$

or

$$k(x_i, x_j) = \exp\left(\frac{\|x_i - x_j\|^2}{2\sigma^2}\right), \quad \text{when } \gamma = \frac{1}{2\sigma^2} \tag{4}$$

where x represents two different classes and γ is a statistical kernel parameter. The same parameters are set for all classifications to eliminate the effects of parameterization.

C. Fast and Adaptive Bidimensional Empirical Mode Decomposition

The main steps of FABEMD are the same as in BEMD [18], [30], but the upper and lower envelopes are estimated using order statistics filters with setting the number of sifting iterations for each BIMFs to one, which is the most crucial advantage of FABEMD to reduce computational complexity [19].

A 2-D array of local maxima and minima points generates a maxima map (LMMAX) and a minima map (LMMIN). Both BEMD and FABEMD use a neighboring window method to find local extrema points. A point with a pixel value strictly higher (lower) than all of its neighbors is considered a local maxima (minima). A 3×3 window yields more favorable local extrema detection results than large window sizes, and therefore is usually adopted [20]. The neighboring points within the window are neglected when extrema points are at the boundaries or corners of images

$$a_{mn} \triangleq \begin{cases} \text{Local Maximum} & \text{if } a_{mn} > a_{kl} \\ \text{Local Minimum} & \text{if } a_{mn} < a_{kl} \end{cases} \tag{5}$$

where $\boldsymbol{a_{mn}}$ is an element of the array located at the mth row and the nth column, and (8) and (9) represent k and l in (7)

$$k = m - \frac{w_{ex} - 1}{2} : Fm + \frac{w_{ex} - 1}{2}, \quad C(k \neq m) \tag{6}$$

$$l = n - \frac{w_{ex} - 1}{2} : Fn + \frac{w_{ex} - 1}{2}, \quad C(l \neq m) \tag{7}$$

where $w_{ex} \times w_{ex}$ is the neighboring window size for detecting extrema points.

In FABEMD, two-order statistics filters, MAX and MIN filters, are used instead of iterative optimization approach in BEMD to create continuous upper and lower envelopes for local extrema, LMMAX, and LMMIN. Order statistics filters are spatial filters based on ordering (ranking) the elements contained within the data area encompassed by the filter. The ranking result determines the response filter of every point. These order statistics filters determine an appropriate window size for envelope estimation.

On the basis of image S_i, the window size of order statistics filters is obtained from LMMAX and LMMIN maps, that is, when $\mathrm{FT}_j = S_i$ and $j = 1$, P_j and Q_j can be derived from the input image S_i. For every local maxima point P_j and local minima point Q_j, the Euclidean distance to the nearest nonzero point is calculated as two arrays of distances that are called adjacent maxima distance array (AMAXDA) and adjacent minima distance array (AMINDA), represented as $\boldsymbol{d_{adj\text{-}max}}$ and $\boldsymbol{d_{adj\text{-}min}}$, respectively. The number of AMAXDA and AMINDA is equal to the number of local maximal and minimal points in the maps P_j and Q_j. The window size of order statistics filters can be selected using the distance values in $\boldsymbol{d_{adj\text{-}max}}$ and $\boldsymbol{d_{adj\text{-}min}}$ from the following four choices:

$$\begin{aligned} w_{\text{en-g}} &= d_1 = \text{minimum}\{\text{minimum}\{d_{\text{adj-max}}\}, \\ &\qquad \text{minimum}\{d_{\text{adj-min}}\}\} \\ w_{\text{en-g}} &= d_2 = \text{maximum}\{\text{minimum}\{d_{\text{adj-max}}\}, \\ &\qquad \text{minimum}\{d_{\text{adj-min}}\}\} \\ w_{\text{en-g}} &= d_3 = \text{minimum}\{\text{maximum}\{d_{\text{adj-max}}\}, \\ &\qquad \text{maximum}\{d_{\text{adj-min}}\}\} \\ w_{\text{en-g}} &= d_4 = \text{maximum}\{\text{maximum}\{d_{\text{adj-max}}\}, \\ &\qquad \text{maximum}\{d_{\text{adj-min}}\}\} \end{aligned} \tag{8}$$

where maximum{} represents the maximal elements in the array, and minimum{} represents the minimal elements in the array. $w_{\text{en-g}}$ is rounded to the nearest odd integer to get the final window size, $w_{\text{en}} \times w_{\text{en}}$.

Once the window size is determined, the intermediate temporary state of BIMF (ITS-BIMF) with corresponding upper and lower envelopes can be obtained by using MAX and MIN filters. The ITS-BIMF value at the jth iteration is denoted as FT_j. The upper envelope ($\boldsymbol{U_E}$) and the lower envelope ($\boldsymbol{L_E}$) are specified as

$$\begin{aligned} U_{Ej}(x, y) &= \mathrm{MAX}_{(s,t)\in Z_{xy}}\{\mathrm{FT}_j(s, t)\} \\ L_{Ej}(x, y) &= \mathrm{MIN}_{(s,t)\in Z_{xy}}\{\mathrm{FT}_j(s, t)\} \end{aligned} \tag{9}$$

where $\boldsymbol{Z_{xy}}$ is the square matrix region $\boldsymbol{w_{en}} \times \boldsymbol{w_{en}}$ at any central point (x, y) of FT_j, and the upper envelope $\boldsymbol{U_{Ej}(x, y)}$ is the array of maximal values in FT_j. Similarly, the lower envelope $\boldsymbol{L_{Ej}(x, y)}$ is the array of minimal values in FT_j. By applying the MAX and MIN filters, new matrices are generated for the upper and lower envelope surfaces from the given data matrix. Then, an averaged smoothing operation is applied and expressed

$$U_{Ej}(x, y) = \frac{1}{w_{sm} \times w_{sm}} \sum_{(s,t)\in Z_{xy}} U_{Ej}(s, t) \tag{10}$$

$$L_{Ej}(x, y) = \frac{1}{w_{sm} \times w_{sm}} \sum_{(s,t)\in Z_{xy}} L_{Ej}(s, t) \tag{11}$$

where $\boldsymbol{Z_{xy}}$ is the square matrix region $\boldsymbol{w_{sm}} = \boldsymbol{w_{sm}}$ at any central point (x, y) of $\boldsymbol{U_{Ej}(x, y)}$ and $\boldsymbol{L_{Ej}(x, y)}$, and $\boldsymbol{w_{sm}}$ is an averaged smoothing window width, and $\boldsymbol{w_{sm}} = \boldsymbol{w_{en}}$. The data operations in (10) and (11) are arithmetic mean filters smoothing local variances, and the average envelope is calculated by using smoothed envelopes $\boldsymbol{U_{Ej}}$ and $\boldsymbol{L_{Ej}}$.

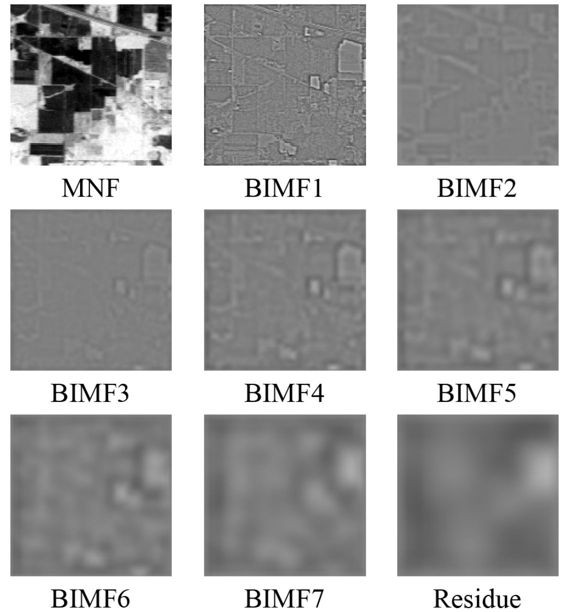

Fig. 2. BIMFs and residue image for MNF 1.

TABLE I
TESTING AND TRAINING PIXELS OF INDIAN PINE HYPERSPECTRAL IMAGE

Class	Training No.	Testing No.	Percentage
alfalfa	10	55	18%
corn-notill	84	1434	6%
corn-min	77	832	9%
corn	33	222	15%
grass/pasture	31	495	6%
grass/trees	42	747	6%
grass/pasture-mowed	4	26	15%
hay-windrowed	18	489	4%
oats	6	20	30%
soybean-notill	63	968	7%
soybean-min	184	2468	7%
soybean-clean	57	613	9%
wheat	20	212	9%
woods	38	1291	3%
bldg-grass-tree-drives	22	380	6%
stone-steel towers	11	95	12%
Total	700	10347	7%

III. RESULTS

A. Study Image

The Indian Pine image acquired from the AVIRIS sensor is broadly used in image classification [31]. The hyperspectral AVIRIS Indian Pine image with ground truth reference is available at https://engineering.purdue.edu/∼biehl/MultiSpec/. The area comprises one-third forest and two-thirds farmland; the image is composed of 145 × 145 pixels, 220 spectral bands, and 16 classes (Fig. 2). The ground truth reference has 10 347 pixels, and 700 pixels (nearly 6.8% of the 10 347 pixels) are used in this letter as training samples for the following tests. The total number of testing and training pixels corresponding to each class is given in Table I.

B. First Step (Dimensional Reduction—MNF Transform)

An MNF transform was performed to reduce noise and dimensions of the Indian Pine image. The output of the MNF

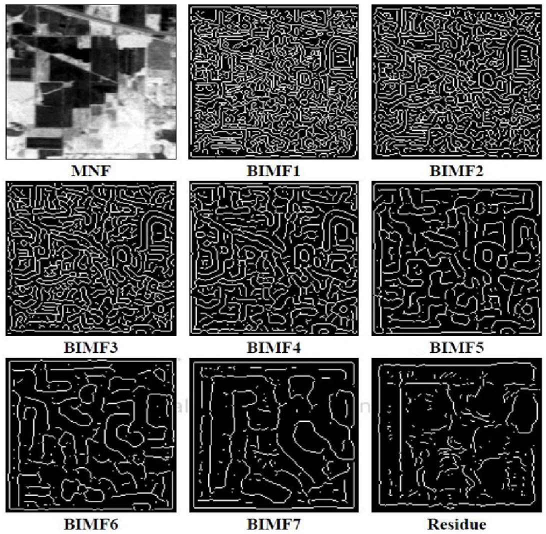

Fig. 3. Results of Canny edge detection for BIMFs in MNF1.

transform comprises new images ordered by SNR ranking and image quality. In general, low-ordered MNF images contain higher SNR and image quality. The first 14 MNF images were extracted to compose three image composites, MNF1–5, MNF1–10, and MNF1–14, for comparison.

C. Second Step (Image Decomposition—FABEMD Process)

In FABEMD, each MNF is decomposed into several BIMFs and a residue image (see Fig. 2 for an example of MNF1). The BIMF has the property of ranking frequency based on BIMF order [32], and the lowest order BIMF has the highest local spatial frequency detail and hence also noise [1]. In addition, Canny edge detection was utilized with a threshold of 0.04 on each BIMF, and the results also support the spatial frequency ranking property of BIMFs (Fig. 3). Therefore, the lower ordered BIMFs with relatively higher spatial frequency details and noise, which not appropriate for classification purpose, were removed. The remainder BIMFs and the residue for each MNF image were fused to generate three image sets, MNF-FABEMD 1–5, MNF-FABEMD 1–10, and MNF-FABEMD 1–14.

D. Classification Evaluation of BIMFs Removal

The numbers of removed BIMFs with corresponding classification accuracy were evaluated for two image sets, MNF-FABEMD 1–10 and MNF-FABEMD 1–14 (Fig. 4). The result of MNF-FABEMD 1–5 was not presented due to the length limitation. The OA and kappa were improved by more than 10% after removing the first two BIMFs for both sets. By removing the first four BIMFs, the accuracy levels increased to 94.8% and 98.1% for MNF-FABEMD 1–10 and MNF-FABEMD 1–14, respectively. Noticeably, the accuracy levels demonstrated steady improvement and reached their peaks when the first four BIMFs were removed. However, the accuracy levels decreased nonsignificantly when the first five or more BIMFs were removed.

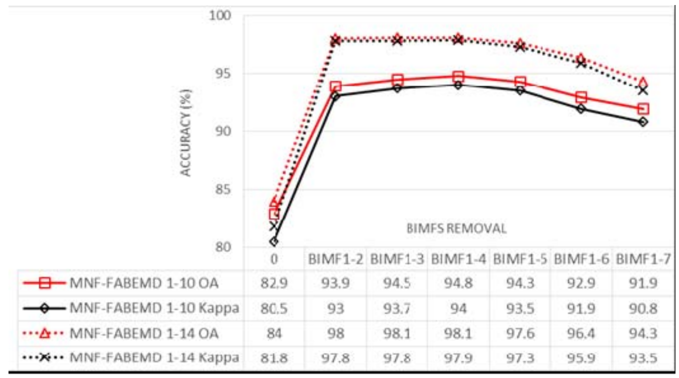

Fig. 4. Classification accuracy of BIMFs removal.

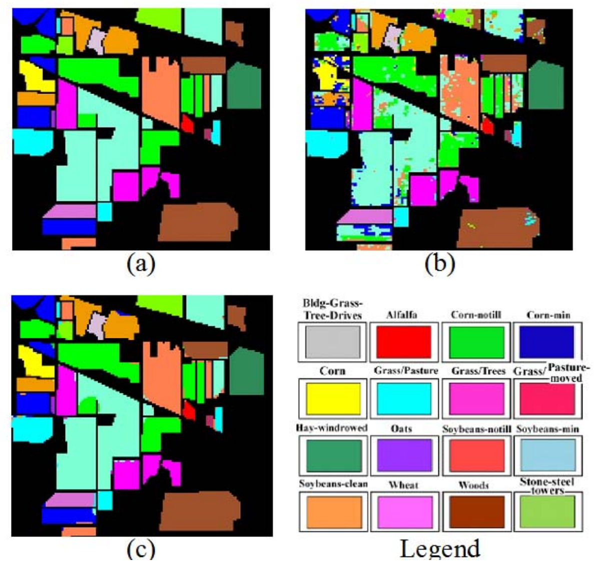

Fig. 5. SVM classification results. (a) Ground truth. (b) MNF1–14. (c) MNF-FABEMD 1–14.

TABLE II
CLASSIFICATION ACCURACY OF MNF SVM AND FABEMD-MNF SVM ON INDIAN PINE HYPERSPECTRAL IMAGE

Method	OA (Kappa)
MNF1-5	69.95% (65.46%)
MNF1-10	84.21% (82.00%)
MNF1-14	84.01% (81.81%)
MNF-FABEMD 1-5	81.39% (78.81%)
MNF-FABEMD 1-10	96.38% (95.86%)
MNF-FABEMD 1-14	98.14% (97.88%)

E. Accuracy Assessment

Three MNF image sets and three MNF-FABEMD image sets were tested for SVM classification, and the results were compared (namely, MNF SVM and MNF-FABEMD SVM).

The accuracy of MNF-FABEMD SVM is higher than that of the MNF SVM (Table II and Fig. 5). The OA were improved from 12% to 81.39% and 96.38% in MNF-FABEMD SVM 1–5 and MNF-FABEMD SVM 1–10, respectively, whereas the OA was improved from 14% to 98.14% in MNF-FABEMD SVM 1–14.

IV. Conclusion

To enhance hyperspectral image classification, this letter proposed a two-step process integrating MNF and FABEMD to reduce image dimension and decompose images. In addition, FABEMD was utilized as a low-pass filter to extract functional informative spectral BIMF images for classification. For the Indian Pine hyperspectral image, the statistically significant OA improvement indicates that the proposed MNF-FABEMD process has superb and stable performance. The major findings can be summarized as follows.

1) The proposed MNF-FABEMD process efficiently eliminated noise and reduced dimensionality in the Indian Pine hyperspectral image. The proposed MNF-FABEMD SVM outperforms the traditional MNF SVM with OA of up to 98.14% and without the need for parameter setting to perform pure spectral classification.
2) To extract sufficient spectral information for optimal classification, this letter evaluated the optimal number of BIMFs to be removed by an exhaustive key search process. The results show that the best classification performance occurred when the first four BIMFs were removed. However, even though the first five or more BIMFs were removed, the accuracy levels of MNF-FABEMD SVM decreased slightly and were higher than that of the MNF SVM, which indicates the stability and improvement of the proposed MNF-FABEMD process in hyperspectral image classification.

At present, the proposed MNF-FABEMD method is a two-step process that may raise a concern about the level of complexity. The exhaustive key search process in determining the optimal number of BIMF to be removed could be improved by developing an index to automatically determine the optimal BIMFs numbers in the further research.

References

[1] B. Demir, S. Ertürk, and M. K. Güllü, "Hyperspectral image classification using denoising of intrinsic mode functions," *IEEE Geosci. Remote Sens. Lett.*, vol. 8, no. 2, pp. 220–224, Mar. 2011.

[2] P. Ghamisi, J. A. Benediktsson, G. Cavallaro, and A. Plaza, "Automatic framework for spectral–spatial classification based on supervised feature extraction and morphological attribute profiles," *IEEE J. Sel. Topics Appl. Earth Observ. Remote Sens.*, vol. 7, no. 6, pp. 2147–2160, Jun. 2014.

[3] X. Huang *et al.*, "Multiple morphological profiles from multicomponent-base images for hyperspectral image classification," *IEEE J. Sel. Topics Appl. Earth Observ. Remote Sens.*, vol. 7, no. 12, pp. 4653–4669, Dec. 2014.

[4] M.-D. Yang, "A genetic algorithm (GA) based automated classifier for remote sensing imagery," *Can. J. Remote Sens.*, vol. 33, no. 3, pp. 203–213, 2007.

[5] M. D. Yang, Y. F. Yang, and S. C. Hsu, "Application of remotely sensed data to the assessment of terrain factors affecting the Tsao–Ling landslide," *Can. J. Remote Sens.*, vol. 30, pp. 593–603, 2004.

[6] I. Dópido, A. Villa, A. Plaza, and P. Gamba, "A quantitative and comparative assessment of unmixing-based feature extraction techniques for hyperspectral image classification," *IEEE J. Sel. Topics Appl. Earth Observ. Remote Sens.*, vol. 5, no. 2, pp. 421–435, Apr. 2012.

[7] M.-D. Yang, T.-C. Su, N.-F. Pan, and Y.-F. Yang, "Systematic image quality assessment for sewer inspection," *Expert Syst. Appl.*, vol. 38, no. 3, pp. 1766–1776, 2011.

[8] V. Bhateja, A. Tripathi and A. Gupta, "An improved local statistics filter for denoising of SAR images," in *Recent Advances in Intelligent Informatics*. Springer, Heidelberg, vol. 235, pp. 23–29, 2014.

[9] P. Brémaud, *Mathematical Principles of Signal Processing: Fourier and Wavelet Analysis*. New York, NY, USA: Springer, 2013.

[10] M.-D. Yang, T.-C. Su, N.-F. Pan, and P. Liu, "Feature extraction of sewer pipe defects using wavelet transform and co-occurrence matrix," *Int. J. Wavelets, Multiresolution Inf. Process.*, vol. 9, no. 2, pp. 211–225, 2011.

[11] J. Xia, P. Du, X. He, and J. Chanussot, "Hyperspectral remote sensing image classification based on rotation forest," *IEEE Geosci. Remote Sens. Lett.*, vol. 11, no. 1, pp. 239–243, Jan. 2014.

[12] M.-D. Yang and T.-C. Su, "Segmenting ideal morphologies of sewer pipe defects on CCTV images for automated diagnosis," *Expert Syst. Appl.*, vol. 36, no. 2, pp. 3562–3573, 2009.

[13] T.-C. Su, M.-D. Yang, T.-C. Wu, and J.-Y. Lin, "Morphological segmentation based on edge detection for sewer pipe defects on CCTV images," *Expert Syst. Appl.*, vol. 38, no. 10, pp. 13094–13114, 2011.

[14] G. Luo, G. Chen, L. Tian, K. Qin, and S.-E. Qian, "Minimum noise fraction versus principal component analysis as a preprocessing step for hyperspectral imagery denoising," *Can. J. Remote Sens.*, vol. 42, no. 2, pp. 106–116, 2016.

[15] N. E. Huang *et al.*, "The empirical mode decomposition and the Hilbert spectrum for nonlinear and non-stationary time series analysis," *Proc. Roy. Soc. London A*, vol. 454, pp. 903–995, Mar. 1998.

[16] Y. Chen, G. Zhang, S. Gan, and C. Zhang, "Enhancing seismic reflections using empirical mode decomposition in the flattened domain," *J. Appl. Geophys.*, vol. 119, pp. 99–105, Aug. 2015.

[17] Y. Chen, C. Zhou, J. Yuan and Z. Jin, "Applications of empirical mode decomposition in random noise attenuation of seismic data," *J. Seism. Explor.*, vol. 23, no. 5, pp. 481–495, Nov. 2014.

[18] Y. Chen and J. Ma, "Random noise attenuation by f-x empirical-mode decomposition predictive filtering," *Geophysics*, vol. 79, no. 3, pp. V81–V91, 2014.

[19] A. Linderhed, "2D empirical mode decompositions in the spirit of image compression," *Proc. SPIE*, vol. 4738, pp. 1–8, Mar. 2002.

[20] S. M. A. Bhuiyan, R. R. Adhami, and J. F. Khan, "Fast and adaptive bidimensional empirical mode decomposition using order-statistics filter based envelope estimation," *EURASIP J. Adv. Signal Process.*, vol. 2008, no. 164, pp. 1–18, Dec. 2008.

[21] C. Cortes and V. Vapnik, "Support-vector networks," *Mach. Learn.*, vol. 20, no. 3, pp. 273–297, 1995.

[22] A. Grigorievskiy, Y. Miche, A.-M. Ventelä, E. Séverin, and A. Lendasse, "Long-term time series prediction using OP-ELM," *Neural Netw.*, vol. 51, pp. 50–56, Mar. 2014.

[23] H. Yu and S. Kim, "SVM tutorial—Classification, regression and ranking," in *Handbook of Natural Computing*, vol. 1. Berlin, Germany: Springer, 2012, pp. 479–506.

[24] G. Kim, B. K. Chae, and D. L. Olson, "A support vector machine (SVM) approach to imbalanced datasets of customer responses: Comparison with other customer response models," *Service Bus.*, vol. 7, no. 1, pp. 167–182, 2013.

[25] M.-D. Yang and T.-C. Su, "Automated diagnosis of sewer pipe defects based on machine learning approaches," *Expert Syst. Appl.*, vol. 35, no. 3, pp. 1327–1337, 2008.

[26] Y. Chai, V. Lempitsky, and A. Zisserman, "BiCoS: A bi-level co-segmentation method for image classification," in *Proc. ICCV*, Nov. 2011, pp. 2579–2586.

[27] R. Hang, Q. Liu, H. Song, and Y. Sun, "Matrix-based discriminant subspace ensemble for hyperspectral image spatial–spectral feature fusion," *IEEE Trans. Geosci. Remote Sens.*, vol. 54, no. 2, pp. 783–794, Feb. 2016.

[28] A. A. Nielsen, "Kernel maximum autocorrelation factor and minimum noise fraction transformations," *IEEE Trans. Image Process.*, vol. 20, no. 3, pp. 612–624, Mar. 2011.

[29] H. Chen, B. Yang, J. Liu, and D. Liu, "A support vector machine classifier with rough set-based feature selection for breast cancer diagnosis," *Expert Syst. Appl.*, vol. 38, pp. 9014–9022, Jul. 2011.

[30] M. Trusiak, M. Wielgus, and K. Patorski, "Advanced processing of optical fringe patterns by automated selective reconstruction and enhanced fast empirical mode decomposition," *Opt. Lasers Eng.*, vol. 52, pp. 230–240, Jan. 2014.

[31] S. Bernabé, P. R. Marpu, A. Plaza, M. Dalla Mura, and J. A. Benediktsson, "Spectral–spatial classification of multispectral images using kernel feature space representation," *IEEE Geosci. Remote Sens. Lett.*, vol. 11, no. 1, pp. 288–292, Jan. 2014.

[32] A. R. Rao and E.-C. Hsu, *Hilbert–Huang Transform Analysis of Hydrological and Environmental Time Series*. Dordrecht, The Netherlands: Springer, 2008.